Phase transitions in biogenic amorphous calcium carbonate

Yutao U. T. Gong[a], Christopher E. Killian[a,b], Ian C. Olson[a], Narayana P. Appathurai[c], Audra L. Amasino[a], Michael C. Martin[d], Liam J. Holt[b], Fred H. Wilt[b], and P. U. P. A. Gilbert[a,e,1,2]

[a]Department of Physics, University of Wisconsin-Madison, 1150 University Avenue, Madison, WI 53706; [b]Department of Molecular and Cell Biology, University of California, Berkeley, CA 94720; [c]Synchrotron Radiation Center, University of Wisconsin-Madison, Stoughton, WI 53589; [d]Advanced Light Source, Lawrence Berkeley National Laboratory, Berkeley, CA 94720; and [e]Department of Chemistry, University of Wisconsin-Madison, 1101 University Avenue, Madison, WI 53706

Edited by Alexandra Navrotsky, University of California, Davis, CA, and approved February 8, 2012 (received for review November 3, 2011)

Crystalline biominerals do not resemble faceted crystals. Current explanations for this property involve formation via amorphous phases. Using X-ray absorption near-edge structure (XANES) spectroscopy and photoelectron emission microscopy (PEEM), here we examine forming spicules in embryos of *Strongylocentrotus purpuratus* sea urchins, and observe a sequence of three mineral phases: hydrated amorphous calcium carbonate ($ACC \cdot H_2O$) → dehydrated amorphous calcium carbonate (ACC) → calcite. Unexpectedly, we find $ACC \cdot H_2O$-rich nanoparticles that persist after the surrounding mineral has dehydrated and crystallized. Protein matrix components occluded within the mineral must inhibit $ACC \cdot H_2O$ dehydration. We devised an in vitro, also using XANES-PEEM, assay to identify spicule proteins that may play a role in stabilizing various mineral phases, and found that the most abundant occluded matrix protein in the sea urchin spicules, SM50, stabilizes $ACC \cdot H_2O$ in vitro.

calcite | synchrotron | larva | echinoderm | echinodermata

Amorphous calcium carbonate (ACC) is an important precursor to geologic and biogenic calcium carbonate ($CaCO_3$) minerals, with natural and industrial relevance including CO_2 sequestration (1), scaling of pipes and desalination membranes (2), and biomineral formation (3). Within the last three years, important discoveries have revealed that $CaCO_3$ aggregates into particles up to 120 nm in size (4), and can grow faster than crystalline calcite (5). Synthetic ACC crystallizes readily, within minutes, particularly when it is in contact with water (6). In contrast, biogenic ACC persists for days in the animal, and months if extracted and stored dry (7).

Among the minerals formed by living organisms, or biominerals (8), the spicules formed by sea urchin larval embryos are widely studied because they are relatively simple biominerals, with 99.9 wt % calcite ($CaCO_3$) and 0.1 wt % proteins (9). In addition, with the publication of the sea urchin genome (10) and spicule proteome, many spicule proteins have been identified and isolated (11), although the functions of any of these proteins during spicule formation have not been identified. Sea urchin spicule mineralization initiates in the gastrula stage embryo (around 30 h postfertilization in *Strongylocentrotus purpuratus*) and takes place in a closed multicellular compartment termed a syncytium (12), with no space or water between the growing spicule mineral and the syncytial membrane (13). Spicule growth does not proceed atom by atom as in classical crystal growth from solution, but uses transient amorphous phases (7), with ACC first packed into 100-nm intracellular vesicles, and then delivered into the syncytial membrane (13). The use of ACC precursors elegantly circumvents the slow processes of crystal nucleation and growth from solution, whereas the exclusion of bulk water from the intracellular vesicles and from the syncytium prevents rapid ACC crystallization.

Sea urchin spicules were long suspected (14), and then confirmed (15, 16) to form via two ACC precursors, one hydrated and one not. Politi et al. (15) analyzed the surfaces of spicules and showed that there are indeed two amorphous mineral precursors in addition to calcite: a hydrated form of ACC, another distinct phase, that at the time was presumed to be anhydrous, and a crystalline calcite phase. These three surface phases, termed type 1 ($ACC \cdot H_2O$), type 2 (ACC), and type 3 (calcite), were observed to coexist and to crystallize with aging, but the precise sequence of transformation could not be identified directly (16). Later Radha et al. (6) showed that the enthalpy of transformation of fresh amorphous spicules, which contain approximately 50% type 2 ACC (14), is similar to the enthalpy of transformation from synthetic anhydrous ACC to crystalline calcite. Politi et al.'s interpretation of type 2 ACC as being anhydrous ACC in spicules, therefore, appeared likely to be correct.

Here we use X-ray absorption near-edge structure (XANES) spectroscopy combined with photoelectron emission spectromicroscopy (PEEM) with unprecedented spatial resolution, and show that in cross-sections of fresh spicules there are indeed the same three mineral phases identified by Politi et al. on spicule surfaces, and that the sequence of transformations is indeed $ACC \cdot H_2O \rightarrow ACC \rightarrow$ calcite, as proposed by Politi et al. (16) and by Radha et al. (6).

Previous studies with apparently contradictory observations have puzzled many scientists that worked on this system: Fresh, forming sea urchin spicules appear to contain amorphous calcium carbonate when observed by infrared spectroscopy (7) as well as when examined with X-ray absorption spectroscopy at the calcium K-edge (15), and L-edge (16). On the other hand, forming spicules appear to be crystalline calcite when examined using Raman microscopy (14), optical microscopy with crossed polarizers (17), and X-ray diffraction (18). In the latter case, the coexistence of an amorphous phase only appears (if at all) as a decrease in intensity of the crystalline peaks (7). How can the same material be simultaneously amorphous and crystalline, depending on the method used to observe it? It has long been suspected that crystalline and amorphous phases coexist, but direct evidence has been elusive. In the present study, XANES-PEEM experiments reconcile previous observations by showing that all phases, amorphous and crystalline, coexist at the nanoscale. Therefore, with the varying sensitivity and resolution of the different methods used previously, one mineral phase, or the other

Author contributions: P.U.P.A.G. designed research; Y.U.T.G., C.E.K., I.C.O., N.P.A., A.L.A., M.C.M., L.J.H., F.H.W., and P.U.P.A.G. performed research; C.E.K., N.P.A., M.C.M., L.J.H., and F.H.W. contributed new reagents/analytic tools; Y.U.T.G., A.L.A., and P.U.P.A.G. analyzed data; and Y.U.T.G., C.E.K., L.J.H., F.H.W., and P.U.P.A.G. wrote the paper.

The authors declare no conflict of interest.

This article is a PNAS Direct Submission.

Freely available online through the PNAS open access option.

[1]To whom correspondence should be addressed. E-mail: pupa@physics.wisc.edu.

[2]Previously published as Gelsomina De Stasio.

This article contains supporting information online at www.pnas.org/lookup/suppl/doi:10.1073/pnas.1118085109/-/DCSupplemental.

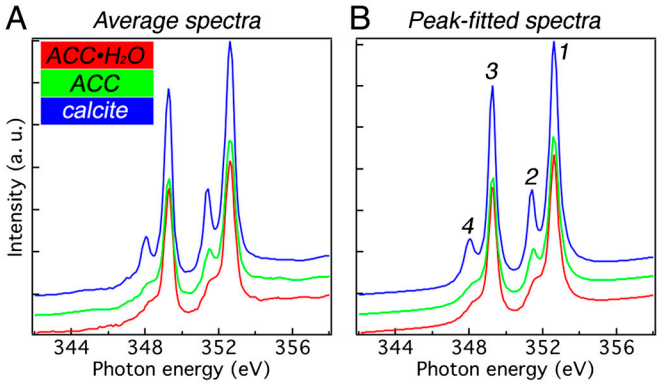

Fig. 1. The three reference spectra used for component analysis. (*A*) XANES spectra across the calcium L-edge extracted from sea urchin spicules. To minimize experimental noise, 6–10 independently acquired single-pixel spectra, with pixel sizes of 20 nm, were averaged to give each reference spectrum. (*B*) Spectra resulting from peak-fitting the spectra in *A*, which completely eliminates experimental noise from these spectra, thus they can be used as reference components for all analyses in this work. The red spectrum is hydrated amorphous calcium carbonate (ACC · H_2O, see Fig. S1), the green spectrum is anhydrous ACC, and the blue spectrum is crystalline calcite, as identified by Politi et al. (16). A comparison of the three spectra highlights that the main peaks labeled 1 and 3 do not vary across the three mineral phases, whereas peaks 2 and 4 do vary. Specifically, in red ACC · H_2O both peaks are low, in green ACC peak 2 is high and peak 4 is low, whereas in calcite both are high. More details on how these spectra were obtained are provided in Fig. S2 and Table S1.

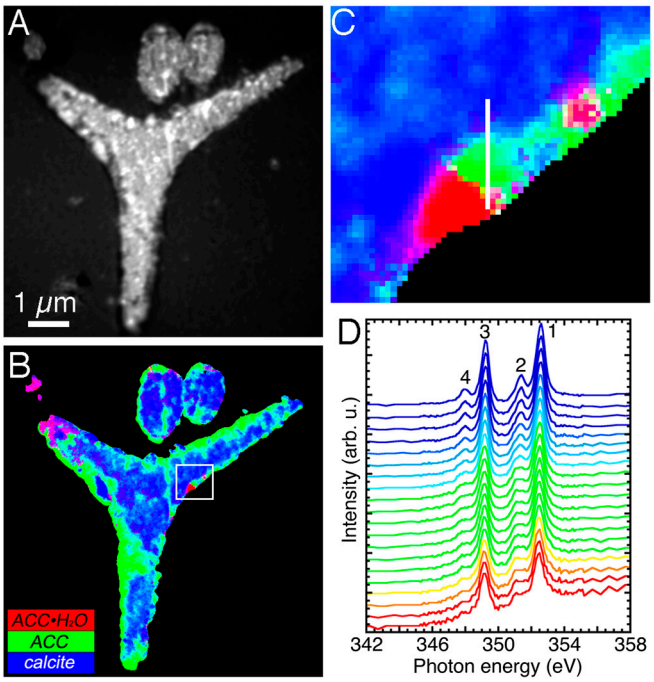

Fig. 2. Component mapping in 48-h spicules, at the prism developmental stage, analyzed within 24 h of extraction from the embryo. (*A*) XANES-PEEM image of three spicules embedded in epoxy, polished to expose a cross-section, and coated. The image is an average of all 121 images acquired across the Ca L-edge. The larger triradiate portion of a spicule at the center is polished in plane, whereas two other cylindrical spicules at the top have their long axes perpendicular to the plane of the image. (*B*) RGB map displaying the results of component mapping, in which each component is color-coded as in Fig. 1. The box indicates the region magnified in *C*. (*C*) Zoomed-in portion of the RGB map in *B*, where each 15-nm pixel shows a different color. Pure phases are R, G, or B, whereas mixed phases are cyan, magenta, or yellow, according to the rules of additive color mixing: G + B = C, R + B = M, R + G = Y (59). The white vertical line shows the positions of the 20 pixels from which the spectra in *D* were extracted. (*D*) Sequence of 20 XANES spectra extracted from 15-nm adjacent pixels along the white line in *C*. The color-coding is the same as used in *B*, *C*, and Fig. 1. Notice that the white line in *C* runs from the outer rim of the spicule (red), passing through orange, yellow, green, cyan, and finally blue, toward the crystalline center of the spicule. Correspondingly, moving from bottom to top across the spectra in *D*, one can see peak-2 growth leading, and peak-4 emergence and growth lagging.

prevails. Unexpected phase mixtures were detected, which led to the discovery of a unique protein function.

Results and Discussion

Mapping $CaCO_3$ Phases in Spicules. Sea urchin spicules were embedded in epoxy, polished to expose their cross-sections, and then coated as described in refs. 19 and 20. Once we identified a spicule with real-time PEEM imaging, we remained on the spicule and acquired stacks of images at varying photon energies, scanning across the calcium L-edge. Typical images had a 20-μm, or smaller, square field of view, and contained 10^6 pixels. Each pixel in a stack of images, therefore, had a size of 20 nm and contained a complete Ca XANES spectrum. With unique data processing software (21) we performed component analysis: We extracted a spectrum from each pixel and measured the proportion of each of the three component spectra shown in Fig. 1 (also see Figs. S1 and S2). The proportions were then displayed as colors in red, green, and blue (RGB) maps as the ones in Figs. 2 and 3 (also see Tables S1 and S2).

We analyzed a total of 83 spicule cross-sections, from three samples, and distinct embryo cultures, extracted 36 h, 48 h, and 72 h after fertilization, respectively, and found consistent results. Fig. 3 shows a representative set of spicules with different orientations, sizes, and developmental stages.

Several observations stand out from the transforming, 48-h spicules in Figs. 2 and 3. First, red pixels, which contain pure ACC · H_2O, are usually localized at the periphery of the spicule, with few or none at the center. This finding is consistent with previous knowledge that new spicule mineral is deposited at the outer edges of the spicule (12, 13). One can conclude that the ACC · H_2O is short lived, and rapidly dehydrates after it is deposited on the spicule surface.

Dehydrated ACC green pixels are much more abundant than ACC · H_2O red pixels, and they too are preferentially localized all around the spicule outlines. Politi et al. (16) also used XANES-PEEM but were only able to analyze the surfaces of intact spicules, rather than cross-sections as presented here. They found that green ACC was the most abundant phase in forming spicules. Here we find 32% ACC in 48-h spicule cross-sections, whereas 72-h spicules do not show any residual green ACC in spicule cross-sections (Fig. 3, Table S2), which is consistent with previous Raman spectroscopy results (14).

Pure calcite blue pixels are concentrated at the center of the spicules. The sequence of spectra acquired going from the outside to the inside of the spicule cross-section (Fig. 2 *C* and *D*) shows the sequence of phase transformations, and their intermediates. This observation supplies direct evidence that the sequence of phase transformations leading to biogenic calcite is indeed ACC · H_2O → ACC → calcite. This sequence of transitions was hypothesized by Raz et al. (14) and Politi et al. (16) and then confirmed to be thermodynamically reasonable by Radha et al. (6). Our studies here directly observe these transitions in time and space in biogenic minerals.

We observe few yellow pixels (Y = R + G = ACC · H_2O + ACC), which is consistent with the paucity of red ACC · H_2O observed, and its short lifetime. There are, however, numerous cyan pixels (C = G + B = ACC + calcite) indicating that ACC in those pixels is transforming to crystalline calcite; but there are also abundant magenta pixels (M = R + B = ACC · H_2O + calcite, Fig. S3) even at the center of the spicules, where most of the mineral is already crystalline. This final observation

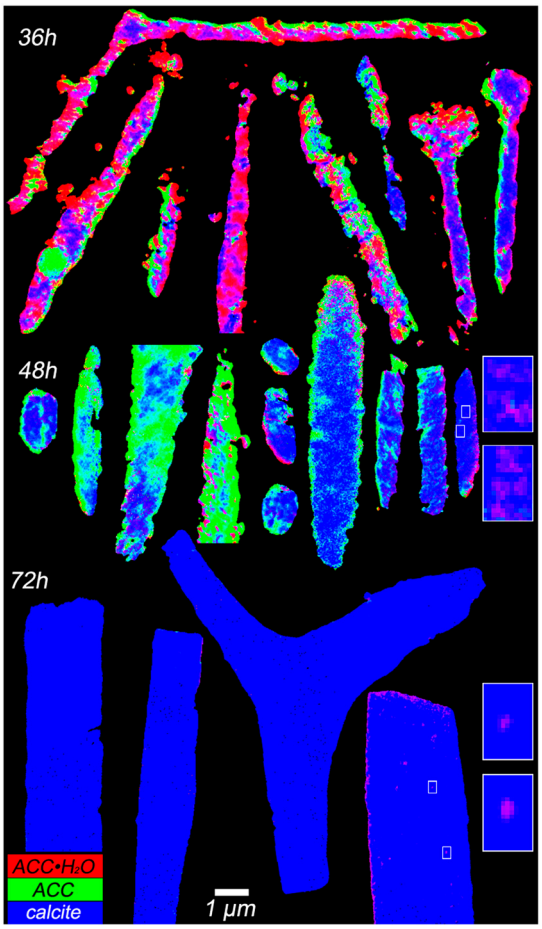

Fig. 3. RGB maps resulting from component analysis done on spicules extracted 36 h, 48 h, and 72 h after fertilization, analyzed within 24 h of extraction from the embryos. Horizontally, the spicules are ordered from most amorphous to most crystalline. Notice the large density of R and B pixels in 36-h, and 72-h spicules, respectively. See Table S2 for a quantitative analysis of R, G, B pixels. In the 48-h spicules R and G pixels, indicating amorphous phases, are always at the outer rims, whereas blue crystalline calcite is always at the center of each cross-section. Also notice that magenta nanoparticles are quite frequent (see spicules on the right, for instance). Magenta nanoparticles are made of colocalized ACC · H_2O and calcite. *Insets* on the right show zoomed-in maps of the four regions in white boxes on the 48-h and 72-h spicules on the right. (*Insets*) Pixels are 20 nm, and the color balance has been adjusted to enhance the magenta nanoparticle, otherwise faint, because magenta nanoparticles contain a much greater proportion of calcite than ACC · H_2O. These nanoparticles are 60–120 nm in size, and are consistently surrounded by blue calcite. See Fig. S3 for further spectroscopic analysis of the magenta nanoparticles.

was unexpected and led us to investigate how the short-lived ACC · H_2O persists in this way.

In Fig. S4 we present additional infrared data showing that spicules become progressively dehydrated as the embryo develops from 48 to 72 h (prism to pluteus stages), and the mineral crystallizes. Each infrared spectrum is strongly averaged over many spicules, and hence has significance for the chemical composition of spicules. The spatial distributions of Figs. 2 and 3 are in agreement with the infrared result, but provide much greater resolution. Notice in particular that in transforming spicules at 48 h the center of the spicules in cross-section is mostly crystalline, whereas amorphous phases tend to be localized at the outer rims.

The Persistence of ACC · H_2O. Given the ACC · H_2O → ACC → calcite sequence of phase transitions established in Fig. 2, it is surprising that we find magenta nanoparticles of ACC · H_2O + calcite in the middle of the spicule cross-sections surrounded by blue calcite and not by green dehydrated ACC (Figs. 2 and 3). The magenta nanoparticles persist 2 mo after extraction from the embryo, as shown in Fig. S5. We hypothesize that there is an inhibiting agent that greatly delays or completely stops the transition from ACC · H_2O → ACC. This inhibitor is likely a protein or proteins because nucleic acids, lipids, and polysaccharides are not found in the spicule (22). We propose that when the inhibitory proteins are trapped in specific locations inside a crystallizing spicule, the ACC · H_2O in those locations cannot dehydrate.

Radha et al. (6) showed recently that both transitions ACC · H_2O → ACC and ACC → calcite have negative enthalpies of transformation. These transitions are energetically favorable and should happen spontaneously with time in the absence of inhibitory molecules. However, the persistence of ACC · H_2O in the magenta nanoparticles suggests that occasionally there is a high activation barrier for the ACC · H_2O → ACC transition perhaps because of proteins that inhibit this transition, thus stabilizing ACC · H_2O. Aizenberg et al. (23, 24) showed a similar function of polyanionic proteins in mollusk shells that stabilize ACC.

Our model simulation shows how the presence of dehydration-inhibiting protein(s) results in islands of ACC · H_2O after crystallization of the spicule (Fig. S6 and Movies S1 and S2). Crystallinity propagates through the fully formed, space-filling (25), three-dimensional anhydrous amorphous phase, following random-walk patterns in three dimensions. This mechanism was first described by Killian et al. (26) in the polycrystalline matrix of the sea urchin tooth, and we believe that it occurs identically in the sea urchin spicules studied here.

Persisting, long-lived nanoparticles of dehydrated ACC (green or cyan) are not found anywhere in spicule cross-sections. This result suggests that the dehydration and crystallization transitions have very different dynamics. These transitions happen in minutes in synthetic ACC, but much more slowly in spicules: Green and red pixels persist 24 h after extraction from the embryo (Figs. 2 and 3–48 h). Both transitions, therefore, must be inhibited in vivo.

In Fig. 3, compared to the newly formed 36-h, and the almost entirely crystalline 72-h, the transforming 48-h spicules are the most revealing to analyze and discuss in depth. Based on the spicules in Fig. 3, and the following considerations, we arrived at a schematic representation of the energy landscape of the ACC · H_2O → ACC → calcite transitions, and the hypothetical activation barriers between them, as presented in Fig. S7. First, the transitions from red to green (dehydration) and from green to blue (crystallization) are thermodynamically downhill (exothermic) (6). Second, the majority of ACC · H_2O is short-lived, as is evident from its paucity in 48-h spicules in Figs. 2 and 3–48 h, and its restriction to the zone of deposition at the outer rims of the spicules in transforming 48-h spicules. The dehydration transition, therefore, must be fast, and correspondingly the activation barrier for ACC · H_2O → ACC must be the smallest. Third, in 48-h spicules there are many more green pixels than there are red pixels (Figs. 2 and 3–48 h). In addition, in 48-h spicules analyzed 4 d after extraction, some green ACC is still detectable (see Fig. S5), therefore the activation barrier for ACC → calcite must be greater than that for ACC · H_2O → ACC. Fourth, in the presence of inhibiting protein(s), the activation barrier becomes much larger, because even 2 mo after extraction the ACC · H_2O in those magenta nanoparticles still had not dehydrated nor crystallized (see Fig. S5).

The Role of SM50 in Stabilizing ACC · H_2O. We devised an assay to identify proteins that stabilize amorphous calcium carbonate mineral forms in vitro. A promising candidate is the sea urchin matrix protein SM50. SM50 is the most prevalent integral matrix protein from sea urchin embryonic spicules, as well as from adult

spines, tests, and teeth (11, 27, 28). An incorrect amino acid sequence for SM50 was originally published in 1987 at the time of the report of the initial cloning of the SM50 gene and its cognate complementary DNA (29, 30). The corrected SM50 amino acid sequence was published in 1991 (31). The SM50 protein is neither glycosylated (32) nor phosphorylated (11, 32), and it has an alkaline pI (31, 32). In fact, SM50 is one of the most alkaline of the spicule matrix proteins (32). Previous studies have also shown that decreasing SM50 protein levels in sea urchin embryos causes spiculogenesis to stop (17, 33). The *Lytechinus pictus* sea urchin ortholog of SM50, designated LSM34, has also been shown to directly interact with mineralizing calcium carbonate (34).

Fig. 4 and Fig. S8 show the spectroscopic results of the in vitro assays for the proteins stabilizing amorphous mineral phases. In this assay, a water droplet dissolves the topmost layers of geologic calcite. If the droplet deposited is just water, then as the droplet dries and the water evaporates, the ion clusters recrystallize as calcite. If, instead, the inhibiting protein is present in the droplet solution, it prevents dehydration and crystallization, thereby making ACC · H_2O the spectroscopically detectable species in the dried droplet.

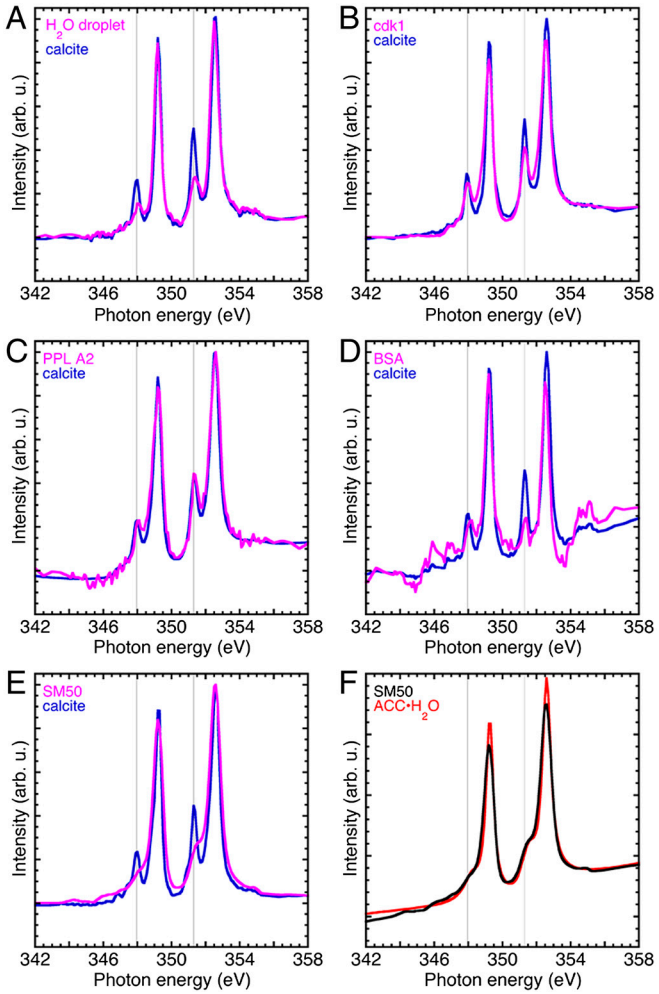

Fig. 4. Ca L-edge spectra acquired with XANES-PEEM on the surface of single-crystal calcite wafers, after depositing a droplet of water or protein in water, and letting it air dry. All data were acquired at the edge of each dried droplet, thus the two spectra in each plot were acquired simultaneously (magenta and blue curves). (*A*) The water droplet suspends a few ions or ion clusters, which then reprecipitate as calcite. The lower intensity crystal field peaks (vertical lines) in the H_2O-dried droplet spectrum indicate a polycrystalline calcite precipitate. (*B*) Cdk1 is a yeast cell cycle kinase expressed and extracted with the same methods used for SM50. This control spectrum also shows calcite reprecipitation. (*C*) PPL A2 is another protein present in sea urchin spicules (11). (*D*) The BSA dried droplet was very thick, hence the Ca signal is weak and noisy, but clearly calcite. (*E*) In the presence of the spicule matrix protein SM50 the reprecipitate is not calcite but hydrated ACC. (*F*) The SM50 spectrum from *E*, overlapped with the fitted ACC · H_2O from Fig. 1*B* (red curve). The two spectra are very similar. Hence we deduce that SM50 stabilizes ACC · H_2O, even in a dried droplet, in ultra-high vacuum, and in direct contact with a crystalline calcite wafer.

We tested SM50 because it is a very prevalent spicule matrix protein. Phospholipase A2 (PPL A2) and cyclin-dependent kinase 1 (cdk1) proteins were tested as controls. PPL A2 from honeybees was used because there is a PPL A2 present in the sea urchin spicule matrix (11). Cdk1 was tested as a control isolated from yeast using the same procedure as the SM50 protein, and because there is no cdk1 in the spicule matrix. This control ensures that the spectroscopic results were not an artifact of the protein preparation. BSA was used as another, non-sea-urchin, non-yeast-prepared control protein.

In Fig. S9 we present Ca and C spectra from all the proteins assayed, confirming that XANES spectroscopy is not simply detecting Ca, but Ca in a cluster of $CaCO_3$ extending at least to the nearest neighboring O atoms in all samples. Only areas of droplet that exhibited both carbonate crystal field peaks in Ca spectra and carbonate π^* peak at 290.3 eV in C spectra were accepted. The latter is a sharp, intense peak distinct from all other peaks in any organic or mineral C-containing species (35). It is impossible that the spectra we interpret as ACC · H_2O are instead single Ca^{2+} ions, each associated with one protein, because these would not show crystal field peaks in Ca spectra, nor a carbonate peak in C spectra, whereas all data presented show both.

The spectra in Fig. 4 show clearly that SM50 stabilizes ACC · H_2O in vitro whereas the other control proteins do not. These findings suggest that SM50 may stabilize ACC · H_2O in sea urchin-mineralized tissues. Because as many as 218 different proteins have been identified in the spicule (11), it is likely that other proteins along with SM50 stabilize ACC · H_2O. SM50 has been found to localize at the outer rim of the spicule (36, 37), where ACC · H_2O stabilization is most important, placing SM50 at the appropriate location in the spicule for it to function as an ACC · H_2O-stabilizing factor. Seto et al. (36), Urry et al. (37), and Killian and Wilt (32) have also detected SM50 occluded at lower density inside the spicule, which is where we observe the magenta nanoparticles. All these observations support the possibility that SM50 stabilizes ACC · H_2O in vivo. SM50 was first cloned 25 years ago (29). However, only in the context of our recent understanding of the dynamics of the mineral phase transformations in sea urchin spicules, and with the advent of powerful spectroscopic and molecular tools, are we now able to decipher SM50's possible function.

Understanding the specific mechanism by which SM50 may stabilize ACC · H_2O is the next challenge. Acidic proteins have long been suspected to play a major role in carbonate biomineralization, and there is much evidence that such proteins stabilize ACC · H_2O (14, 23, 24, 38). SM50, however, is not an acidic protein (31, 32).

The function of only a few biomineral proteins has been identified thus far. Suzuki et al. (39) isolated a protein called Pif that is essential for mollusk shell nacre formation. Starmaker is a protein expressed in zebrafish, which Nicolson and coworkers (40) have shown to be necessary for aragonite polymorph selection, and morphology in the zebrafish otolith. Notwithstanding this paucity of functional analyses, amorphous mineral phases are widespread in biominerals. Therefore the role of proteins acting as inhibitors of phase transition is probably not restricted to sea urchin spicules. Amorphous mineral phases have been identified in forming biominerals from different phyla: echinoderms (7, 16, 26, 41), mollusks (42–44), crustaceans (38, 45–51), annelids (52–54), porifera (55), urochordates (24, 56), and chordates (57, 58). Therefore, the phase transitions and their regulation by

organic molecules observed here may be shared by numerous $CaCO_3$-mineralizing organisms. Biomineralization is a major mechanism of carbon sequestration and therefore a better understanding of this process is of major biogeochemical, environmental, and economic importance.

Methods

Detailed methods are described in *SI Methods*. Sea urchin spicules from 36 h, 48 h, and 72 h embryos were extracted, embedded in epoxy, polished to expose spicule cross-sections, coated with 1-nm Pt in the area to be analyzed by XANES-PEEM, and 40-nm Pt around it (19). They were then analyzed with PEEM-3 on beamline 11.0.1 at the Berkeley-Advanced Light Source. A stack of images was collected across the Ca L-edge, between 340 and 360 eV photon energy (121 images, with field of view either 15×15 μm or 20×20 μm images, 10^6 pixels per image, and pixel sizes 15-nm or 20-nm, respectively), with a sample voltage of −15 kV. Each pixel in a stack contained the complete Ca XANES spectrum, and was fit to a linear combination of the three component spectra in Fig. 1, with proportions of the three components as the fit parameters. The resulting three numbers per pixel were then displayed as RGB maps in Adobe Photoshop, so that pure phases appear red, green, or blue, and mixed phases have intermediate colors, according to additive color mixing rules (59). Each spicule was analyzed in duplicate or triplicate, with reproducible results. Radiation damage, as described in Fig. S10, was prevented by keeping exposure times short.

The assay to test protein functions in vitro was done by depositing 1-μL droplets of 0.1 μg/μL protein solution on the surface of calcite wafers. Control droplets contained only water. Once the droplet had air-dried, the calcite wafer was inserted into ultra-high vacuum (10^{-10} Torr) and analyzed with SPHINX (60) (also a XANES-PEEM) at the Synchrotron Radiation Center. Ca and C spectra from the dried droplet and the surrounding calcite were analyzed simultaneously, and compared. Only areas of droplets that exhibited carbonate features in both Ca and C spectra were accepted. Water and all single proteins except for SM50 reprecipitated calcite, spicule matrix proteins reprecipitated ACC as expected (14), whereas SM50 reprecipitated ACC · H_2O.

ACKNOWLEDGMENTS. We thank Benjamin Gilbert for developing the Gilbert Group Macros (GG-Macros), Andreas Scholl, Anthony Young, and Andrew Doran for their assistance during the experiments on PEEM-3 at the Advanced Light Source (ALS), and Howard Padmore and Richard Celestre for their support in setting up a sample preparation laboratory, enabling fresh spicules to be prepared near the ALS. We thank Elia Beniash and Adam F. Wallace for discussions, and Lia Addadi and Steve Weiner for their valuable criticism of the manuscript. This work was supported by Department of Energy (DOE) Award DE-FG02-07ER15899, National Science Foundation (NSF) Awards CHE-0613972 and DMR-1105167, and University of Wisconsin-Hamel Award (to P.U.P.A.G.). L.J.H. is supported by a Bowes Research Fellows Award. The experiments on spicules were performed at the Berkeley-Advanced Light Source, supported by DOE under contract DE-AC02-05CH11231, those on proteins were done at the Synchrotron Radiation Center, which is funded by NSF Award DMR-0537588, and the University of Wisconsin-Madison and operated by the Graduate School of the University of Wisconsin-Madison.

1. Lackner KS (2003) A guide to CO_2 sequestration. *Science* 300:1677–1678.
2. Sheikholeslami R (2003) Mixed salts—scaling limits and propensity. *Desalination* 154:117–127.
3. Weiner S, Sagi I, Addadi L (2005) Choosing the crystallization path less traveled. *Science* 309:1027–1028.
4. Pouget EM, et al. (2009) The initial stages of template-controlled CaCO(3) formation revealed by cryo-TEM. *Science* 323:1455–1458.
5. Raiteri P, Gale JD (2010) Water is the key to nonclassical nucleation of amorphous calcium carbonate. *J Am Chem Soc* 132:17623–17634.
6. Radha AV, Forbes TZ, Killian CE, Gilbert PUPA, Navrotsky A (2010) Transformation and crystallization energetics of synthetic and biogenic amorphous calcium carbonate. *Proc Natl Acad Sci USA* 107:16438–16443.
7. Beniash E, Aizenberg J, Addadi L, Weiner S (1997) Amorphous calcium carbonate transforms into calcite during sea urchin larval spicule growth. *Proc R Soc Lond B Biol Sci* 264:461–465.
8. Lowenstam HA, Weiner S (1989) *On Biomineralization* (Oxford Univ Press, Oxford) p 324.
9. Wilt F (1999) Matrix and minerals in the sea urchin larval skeleton. *J Struct Biol* 126:216–226.
10. Consortium SUGS, et al. (2006) The genome of the sea urchin *Strongylocentrotus purpuratus*. *Science* 314:941–952.
11. Mann K, Wilt FH, Poustka A (2010) Proteomic analysis of sea urchin (*Strongylocentrotus purpuratus*) spicule matrix. *Proteome Sci* 8:33.
12. Wilt FH (2002) Biomineralization of the spicules of sea urchin embryos. *Zool Sci* 19:253–261.
13. Beniash E, Addadi L, Weiner S (1999) Cellular control over spicule formation in sea urchin embryos: A structural approach. *J Struct Biol* 125:50–62.
14. Raz S, Hamilton PC, Wilt FH, Weiner S, Addadi L (2003) The transient phase of amorphous calcium carbonate in sea urchin larval spicules: The involvement of proteins and magnesium ion in its formation and stabilization. *Adv Funct Mater* 13:480–486.
15. Politi Y, et al. (2006) Structural characterization of the transient amorphous calcium carbonate precursor phase in sea urchin embryos. *Adv Funct Mater* 16:1289–1298.
16. Politi Y, et al. (2008) Transformation mechanism of amorphous calcium carbonate into calcite in the sea urchin larval spicule. *Proc Natl Acad Sci USA* 105:17362–17366.
17. Wilt FH, Croker L, Killian CE, McDonald K (2008) The role of LSM34/SpSM50 in endoskeletal spicule formation in sea urchin embryos. *Invert Biol* 127:452–459.
18. Berman A, et al. (1993) Biological-control of crystal texture—a widespread strategy for adapting crystal properties to function. *Science* 259:776–779.
19. De Stasio G, Frazer BH, Gilbert B, Richter KL, Valley JW (2003) Compensation of charging in X-PEEM: A successful test on mineral inclusions in 4.4 Ga old zircon. *Ultramicroscopy* 98:57–62.
20. Gilbert PUPA, Frazer BH, Abrecht M (2005) The organic-mineral interface in biominerals. *Molecular Geomicrobiology*, Reviews in Mineralogy and Geochemistry, eds JF Banfield, KH Nealson, and J Cervini-Silva (Mineralogical Society of America, Washington, DC), Vol 59, pp 157–185.
21. GG-Macros., http://home.physics.wisc.edu/gilbert/.
22. Benson SC, Benson NC, Wilt F (1986) The organic matrix of the skeletal spicule of sea-urchin embryos. *J Cell Biol* 102:1878–1886.
23. Aizenberg J, Lambert G, Addadi L, Weiner S (1996) Stabilization of amorphous calcium carbonate by specialized macromolecules in biological and synthetic precipitates. *Adv Mater* 8:222–226.
24. Aizenberg J, Lambert G, Weiner S, Addadi L (2002) Factors involved in the formation of amorphous and crystalline calcium carbonate: A study of an ascidian skeleton. *J Am Chem Soc* 124:32–39.
25. Yang L, Killian CE, Kunz M, Tamura N, Gilbert PUPA (2011) Biomineral nanoparticles are space-filling. *Nanoscale* 3:603–609.
26. Killian CE, et al. (2009) The mechanism of calcite co-orientation in the sea urchin tooth. *J Am Chem Soc* 131:18404–18409.
27. Mann K, Poustka AJ, Mann M (2008) In-depth, high-accuracy proteomics of sea urchin tooth organic matrix. *Proteome Sci* 6:33.
28. Mann K, Poustka AJ, Mann M (2008) The sea urchin (*Strongylocentrotus purpuratus*) test and spine proteomes. *Proteome Sci* 6:22.
29. Benson S, Sucov H, Stephens L, Davidson E, Wilt F (1987) A lineage-specific gene encoding a major matrix protein of the sea-urchin embryo spicule. I. Authentication of the cloned gene and its developmental expression. *Dev Biol* 120:499–506.
30. Sucov H, et al. (1987) A lineage-specific gene encoding a major matrix protein of the sea urchin embryo spicule. II. Structure of the gene and derived sequence of the protein. *Dev Biol* 120:507–519.
31. Katoh-Fukui Y, et al. (1991) The corrected structure of the SM50 spicule matrix protein of *Strongylocentrotus purpuratus*. *Dev Biol* 145:201–202.
32. Killian CE, Wilt FH (1996) Characterization of the proteins comprising the integral matrix of *Strongylocentrotus purpuratus* embryonic spicules. *J Biol Chem* 271:9150–9159.
33. Peled-Kamar M, Hamilton P, Wilt FH (2002) The spicule matrix protein LSM34 is essential for biomineralization of the sea urchin spicule. *Exp Cell Res* 272:56–61.
34. Metzler RA, et al. (2008) Probing the organic-mineral interface at the molecular level in model biominerals. *Langmuir* 24:2680–2687.
35. Metzler RA, et al. (2008) Polarization-dependent imaging contrast in abalone shells. *Phys Rev B* 77:064110.
36. Seto J, Zhang Y, Hamilton P, Wilt F (2004) The localization of occluded matrix proteins in calcareous spicules of sea urchin larvae. *J Struct Biol* 148:123–130.
37. Urry LA, Hamilton PC, Killian CE, Wilt FH (2000) Expression of spicule matrix proteins in the sea urchin embryo during normal and experimentally altered spiculogenesis. *Dev Biol* 225:201–213.
38. Levi-Kalisman Y, Raz S, Weiner S, Addadi L, Sagi I (2000) X-Ray absorption spectroscopy studies on the structure of a biogenic "amorphous" calcium carbonate phase. *J Chem Soc Dalton Trans* 3977–3982.
39. Suzuki M, et al. (2009) An acidic matrix protein, Pif, is a key macromolecule for nacre formation. *Science* 325:1388–1390.
40. Söllner C, et al. (2003) Control of crystal size and lattice formation by starmaker in otolith biomineralization. *Science* 302:282–286.
41. Politi Y, Arad T, Klein E, Weiner S, Addadi L (2004) Sea urchin spine calcite forms via a transient amorphous calcium carbonate phase. *Science* 306:1161–1164.
42. Weiss IM, Tuross N, Addadi L, Weiner S (2002) Mollusc larval shell formation: Amorphous calcium carbonate is a precursor phase for aragonite. *J Exp Zool* 293:478–491.
43. Marxen JC, Becker W, Finke D, Hasse B, Epple M (2003) Early mineralization in *Biomphalaria glabrata*: Microscopic and structural results. *J Mollus Stud* 69:113–121.
44. Bentov S, Weil S, Glazer L, Sagi A, Berman A (2010) Stabilization of amorphous calcium carbonate by phosphate rich organic matrix proteins and by single phosphoamino acids. *J Struct Biol* 171:207–215.
45. Vinogradov AP (1953) *The Elementary Chemical Composition of Marine Organisms.* (Yale Univ Press, New Haven, CT).
46. Dillaman R, Hequembourg S, Gay M (2005) Early pattern of calcification in the dorsal carapace of the blue crab, *Callinectes sapidus*. *J Morphol* 263:356–374.
47. Neues F, Ziegler A, Epple M (2007) The composition of the mineralized cuticle in marine and terrestrial isopods: A comparative study. *CrystEngComm* 9:1245–1251.
48. Raz S, Testeniere O, Hecker A, Weiner S, Luquet G (2002) Stable amorphous calcium carbonate is the main component of the calcium storage structures of the crustacean *Orchestia cavimana*. *Biol Bull* 203:269–274.

49. Becker A, et al. (2003) Structural characterisation of X-ray amorphous calcium carbonate (ACC) in sternal deposits of the crustacea *Porcellio scaber*. *Dalton Trans* 4:551–555.
50. Becker A, Ziegler A, Epple M (2005) The mineral phase in the cuticles of two species of Crustacea consists of magnesium calcite, amorphous calcium carbonate, and amorphous calcium phosphate. *Dalton Trans* 10:1814–1820.
51. Chave KE (1954) Aspects of the biogeochemistry of magnesium I. Calcareous marine organisms. *J Geol* 62:266–283.
52. Darwin C (1881) *The Formation of Vegetable Mould, Through the Action of Worms, with Observations on Their Habits* (John Murray, London).
53. Gago-Duport I, Briones MJ, Rodriguez JB, Covelo B (2008) Amorphous calcium carbonate biomineralization in the earthworm's calciferous gland: Pathways to the formation of crystalline phases. *J Struct Biol* 162:422–435.
54. Lee MR, Hodson ME, Langworthy G (2008) Earthworms produce granules of intricately zoned calcite. *Geology* 36:943–946.
55. Sethmann I, Worheide G (2008) Structure and composition of calcareous sponge spicules: A review and comparison to structurally related biominerals. *Micron* 39:209–228.
56. Lambert G, Lambert CC, Lowenstam HA (1990) *Skeletal Biomineralization: Patterns, Processes and Evolutionary Trends*, ed JG Carter (Van Nostrand Reinhold, New York), Vol 1, pp 461–469.
57. Mahamid J, Sharir A, Addadi L, Weiner S (2008) Amorphous calcium phosphate is a major component of the forming fin bones of zebrafish: Indications for an amorphous precursor phase. *Proc Natl Acad Sci USA* 105:12748–12753.
58. Beniash E, Metzler RA, Lam RSK, Gilbert PUPA (2009) Transient amorphous calcium phosphate in forming enamel. *J Struct Biol* 166:133–143.
59. Gilbert PUPA, Haeberli W (2011) *Physics in the Arts, Revised Edition* (Elsevier-Academic, Burlington, MA).
60. Frazer BH, Girasole M, Wiese LM, Franz T, De Stasio G (2004) Spectromicroscope for the photoelectron imaging of nanostructures with X-rays (SPHINX): Performance in biology, medicine and geology. *Ultramicroscopy* 99:87–94.

Supporting Information

Gong et al. 10.1073/pnas.1118085109

SI Text

A Model for Phase Transitions in Sea Urchin Spicules. This model simulation was performed using MATLAB and is based on the following hypotheses:

1. The spicule is a two-dimensional matrix of small squares.
2. Before anything is deposited, the color of the small square is black. The color of each small square indicates the type of component [amorphous calcium carbonate (ACC) · H_2O, red; ACC, green; calcite, blue].
3. If there are mixed phases, the color will reflect the mixture of red, green, and blue (RGB), according to the additive color mixing rules.
4. Initially 4,500 small squares are deposited in an oval shape. Additional squares are added at the outer rim of the oval simulating a spicule cross-section growing in girth. The final number of squares is 18,000.
5. Only ACC · H_2O is deposited in the initial oval and at its growing surface.
6. With time, ACC · H_2O gradually transforms into ACC with transition rate a, defined as $[\text{ACC} \cdot \text{H}_2\text{O}] = e^{-at}$, where $[\text{ACC} \cdot \text{H}_2\text{O}]$ is the concentration of ACC · H_2O in each small square.
7. With time, ACC gradually transforms into calcite with transition rate b, with the concentration of ACC decaying as $[\text{ACC}] = e^{-bt}$. In the model we assumed $a > b$, thus the ACC · H_2O → ACC transition is faster than the ACC → calcite transition. (The time t varies between 0 and 100, $a = 0.2$, $b = 0.02$.)
8. If at least one immediately adjacent square is at least 50% calcite, then an ACC square will transform to calcite faster ($b = 0.04$).
9. In the presence of inhibitor, ACC · H_2O will not transform into ACC. The randomly distributed inhibitors are present in only 1% of the pixels, and each inhibitor affects a 3 × 3 pixel region.

The first seven hypotheses are minimal and simply describe how the model works. The sequence of ACC · H_2O → ACC → calcite transformations assumed in hypotheses 6 and 7 is deduced from the series of spectra in Fig. 2, and supported by the microcalorimetry experiments reported by Radha et al. (1). In hypothesis 7 we assumed $a > b$, so that the ACC · H_2O → ACC transition is fast, whereas the ACC → calcite transition is slow, for consistency with the observations made in Figs. 2 and 3 that ACC · H_2O is short lived (from a few minutes to a few hours, but not days), and that ACC is longer lived (up to a few days at most, as shown in Fig. S5). Hypothesis 8 is based on secondary nucleation, that is, crystallization of an amorphous phase by contact with an already crystallized phase, as first demonstrated by Killian et al. (2).

Hypothesis 9 is central to the model because it is the crux of what is being tested. Thus in the presence of an inhibitor, ACC · H_2O will not transform into ACC, and the pixels containing it will remain red. We did not simulate the existence of an ACC → calcite strong inhibitor because green ACC nanoparticles surrounded by blue calcite were not observed experimentally.

In Fig. S6 we present the results of the model simulations, with and without the ACC · H_2O → ACC inhibitor. The two maps are similar in most aspects observed experimentally in Figs. 2, 3, and S5. The existence of ACC · H_2O nanoparticles, red small squares, is observed only when the inhibitor of ACC · H_2O → ACC transition is added to the model. The similarity of the model results of Fig. S6 and the experimental results in Figs. 2, 3, and S5 suggests strongly that an inhibitor causes the persistence of ACC · H_2O nanoparticles in the forming spicule.

SI Methods

Extraction of Spicules. Fresh sea urchin spicules were extracted from *Strongylocentrotus purpuratus* embryos, grown in filtered natural sea water containing gentamycin (20 mg L^{-1}) at 15 °C, following established methods (3). Spicules were harvested from late-gastrula stage (36 h postfertilization) embryos, from prism stage (48 h postfertilization) embryos, and pluteus stage (72 h postfertilization) embryos. To isolate the spicules, embryos were first centrifuged at 200 × *g* for 5 min and resuspended in distilled water. The embryos were pelleted at 200 × *g* for 5 min. The pelleted embryos were then resuspended in 10 mM Tris (pH 11) and pelleted again at 200 × *g* for 5 min. The pelleted embryos were resuspended in 10 mM Tris (pH 11) and then disrupted using a Techmar (Polytron style) homogenizer for 1 min at approximately 70% power. SDS was added to the homogenate to a 0.1% (wt/vol) concentration and the resulting mixture was centrifuged at 3,700 × *g* for 5 min. The pellet was resuspended in 10 mM Tris (pH 11) using a glass dounce homogenizer, by a few passes of the pestle. The resuspended pellet was again centrifuged at 3,700 × *g* for 5 min. The pelleted spicules were light brown in color at this stage because they contained cellular debris. The spicules were then washed one more time with 10 mM Tris (pH 11), and then twice with 100% ethanol. The spicules were then gently pelleted and stored on dry ice until they were embedded. We did not use bleach to clean the spicules as is usually done in spicule extraction. We find that the remaining organic material surrounding the spicules is desirable because it greatly improves the stability of ACC · H_2O at the outer rim of spicule cross-sections. At the time of embedding, (within 1–2 h after isolation), the spicules were brought back to room temperature, embedded in epoxy (EpoFix, Electron Microscopy Science). Once cured overnight, the blocks were polished with 50-nm alumina grit (MasterPrep, Buehler). Prior to polishing, the alumina suspension was dialyzed against a 22 g/L solution of Na_2CO_3 in double distilled (DD)-H_2O for 24 h, with three solution changes. This step is important to prevent spicule-ACC dissolution during wet polishing. An ethanol droplet was deposited and let dry on the polished spicule cross-sections, to stabilize the metastable phases (4). The samples were then sputter-coated with 1 nm in the area to be analyzed by X-photoelectron emission spectromicroscopy (PEEM), and 40 nm Pt around it, to provide electrical conductivity to the otherwise insulating crystals (5). All spicules were analyzed by X-ray absorption near-edge structure (XANES)-PEEM within 24 h of extraction from the embryos. The spicule in Fig. S4 was analyzed 4 d and again 2 mo after extraction.

Expression and Isolation of SM50 from *Saccharomyces cerevisiae*. The full-length coding region of the *Strongylocentrotus purpuratus* SM50 gene as well as linker regions at its upstream and downstream ends was generated employing RT-PCR using the One-Step RT-PCR kit from Qiagen. The upstream and downstream primer oligonucleotides used were 5′-GGAATTCCAGCTGACCACCATGAAGGGAGTTTTGTTTATTGTGG-3′ and 5′-CGATCCCCGGGAATTGCCATGTGCCAACGCGTCTGCC-3′. The RNA used was total RNA isolated from *S. purpuratus* 48 h prism stage embryos at a concentration of 0.1 μg/μL. After the full-length SM50 coding region plus linker regions were confirmed correct by DNA sequencing, a region of DNA that

encodes a C terminus tandem affinity purification (TAP) tag (6) was added onto the *SM50* coding region using PCR with the primers 5′-GTATCAACAAAAAATTGTTAATATACCTCTATACTTTAACGTCAAGGAGAAGGAATTCCAGCTGACCACC-3′ and 5′-AGCGGTTGGCTGCTGAGACGGCTATGAAATTCTTTTTCCATCTTCTCTTCGATCCCCGGGAATTGCCATG-3′. The resulting amplicon was then cotransformed into competent *S. cerevisiae* W303 MAT a cells with BamHI- and HindIII-restricted pRSAB1234 plasmid (a gift from Erin K. O'Shea, Harvard University, Cambridge, MA). Transformant colonies were picked and grown up to assay for TAP-SM50 protein expression. A single colony of yeast-expressing TAP-SM50 was picked and a larger scale 2 L culture was grown up to $OD_{600} = 0.6$ at 30 °C, 200 rpm, in synthetic minimal media (ura-) with 2% raffinose as a carbon source and then induced with 2% galatose following standard methods. The induced yeast cells were pelleted and lysed using Y-PER lysis buffer (Thermo Scientific) according to manufacturer's instructions. The resulting soluble fraction of the lysate was mixed with IgG-agarose (Sigma-Aldrich), which bound the soluble TAP-tagged SM50. The resin containing TAP-SM50 was washed extensively with TBS (10 mM Tris, pH 7.5, 100 mM NaCl). SM50 was then released from the resin by digestion with ProTev protease (Promega). The unbound solute was then mixed with a Ni-nitrilotriacetate (NTA)-agarose (Qiagen) to remove the His-tagged ProTev protease. The unbound solute from the Ni-NTA-agarose was collected and dialyzed extensively against deionized water. The resulting sample was then examined by SDS-PAGE and Western blotting techniques using SM50 specific antibodies. The soluble SM50 protein concentration was then adjusted to approximately 0.1 μg/μL and quick-frozen until used.

Extraction of Spicule Matrix Proteins (SMPs). The SMPs used for the in vitro assay of protein functions in Figs. 5 and S7 were extracted from 48 h (prism stage) and 72 h (pluteus stage) *S. purpuratus* embryos as described by Rahda et al. (1). Dry spicules, 1–3 mg, were suspended in approximately 500 μL of dH_2O in 2 mL microfuge tubes. The spicules were demineralized by the gradual dropwise addition of glacial acetic acid while the tubes were kept cold on ice and the suspension thoroughly mixed by trituration. Once the mineral of the spicules was visibly dissolved, the samples were then dialyzed extensively versus dH_2O. Insoluble material was removed from the samples by centrifugation at $15{,}000 \times g$ for 15 min. The SMP samples were then quick-frozen and concentrated using lyophilization. The samples were then adjusted in concentration to 0.3 μg/μL and frozen again until use. There was detectable Ca, when the SMPs were deposited on silicon wafers and analyzed with XANES-PEEM. The mineral form detected was consistently dehydrated-ACC, which we presume is a result of extraction from the spicules or sample preparation, and not from the underlying calcite crystal in the experiment of Fig. S7. In 48 h SMPs there were only trace amounts of Ca, whereas in 72 h SMPs there was much more.

In Vitro Assay Accessing the Stabilization of Calcium Carbonate Mineral Forms. Geologic single crystal calcite wafers 10 mm × 10 mm × 1 mm in size were purchased from MTI Corporation. One-microliter droplets of $DD-H_2O$ or $DD-H_2O$ containing proteins were deposited on the calcite wafers and let dry. Three droplets per wafer were deposited, containing 0.1 μg/μL protein solutions. The proteins were: 48-h SMP and 72-h SMP described above. Cyclin-dependent kinase 1 (cdk1) is a yeast cell cycle protein, which was expressed in *S. cerevisiae*, extracted and purified similarly to SM50, to serve as a control for the protein isolation methods employed here. The other proteins were commercially available, and included: BSA (Sigma-Aldrich), which is not a Ca-binding protein and was chosen to be a nonspecific control; phospholipase A2 (PPL A2), the sea urchin spicule matrix contains a PPL A2 (7), although the one we used here was isolated from honeybee venom (Sigma-Aldrich), and therefore, has a different amino acid sequence.

The dried droplets on calcite were analyzed using the SPHINX microscope. Once an image was obtained and the edge of a droplet identified, stacks of images were acquired across the Ca L-edge, thus each stack contained both calcite wafer and dried droplet pixels, analyzed simultaneously. Pairs of spectra selected from a few pixels in both regions are presented in Figs. 5 and S7.

All proteins measured on calcite with this assay were also measured on Si wafers, to make sure that they did not contain any Ca, none of the single proteins did. The protein mixtures in the 48-h and 72-h SMPs showed a Ca signal in XANES-PEEM analysis. In both cases the mineral form detected was positively identified as dehydrated-ACC, which we presume came from the mineral of the spicules during the isolation of these proteins. In 48-h SMP there were only trace amounts of Ca, whereas in 72-h SMP there was more Ca. The observation of residual ACC from spicules in SMPs is consistent with their in vitro function of stabilizing ACC, as shown in the data of Fig. S7, and consistent with the results of Raz et al. (8).

XANES-PEEM Analysis. Ca mapping was done using the PEEM-3 microscope (9) on beamline 11.0.1 at the Advanced Light Source (ALS) at Lawrence Berkeley National Laboratory, and spectra for the in vitro assay of protein function were done at the Synchrotron Radiation Center (SRC) installed on two different beamlines: the high-energy resolution monochromator (HERMON), and the varied-line spacing plane grating monochromator (VLS-PGM) beamlines. Both beamlines used the SPHINX microscope (10).

For calcium mapping we acquired stacks of 121 images of the same 20-μm field of view, or smaller, with 20-nm pixels, acquired while scanning the photon energy across the Ca L-edge, from 340 to 360 eV, with step 0.1 eV between 345–355 eV, and step 0.5 eV elsewhere. Each pixel in a stack, therefore, contains the full Ca-L-edge spectrum. All spicule spectra were acquired using circularly polarized X-rays to eliminate any possible linear dichroism effects.

Reference Spectra. Each reference spectrum (Fig. 1) was obtained by averaging several single-pixel spectra extracted from different stacks, acquired from 36 or 72 h spicules. This procedure was important to eliminate nonstatistical intensity fluctuations, which occur in each stack of images. In Fig. S2 we present all the single-pixel spectra used, along with their average, and the peak-fitted version of the average spectra. Table S1 shows all fit parameters, and provides a quantitative measure of the peaks 2 and 4 enhancement and shift toward lower energy displayed graphically in Fig. S2.

Component Mapping. For the component mapping in Figs. 2, 3, and S5 we used macros developed in the Gilbert Group, called GG Macros, which run in Igor Pro 6.22, and can be downloaded free of charge from ref. 11. Briefly, using these macros we extract a Ca spectrum from each pixel in a stack, and let the software find the best fit of that spectrum using a linear combination of three predetermined spectral components (Fig. 1) and a third order polynomial. We enforce positivity of the spectral components, and allow the spectra to change energy position within a user-specified window, typically less than 1 eV. The result of this fit is a set of three numbers for each pixel, that is, the proportion (between 0 and 1) of each component present in that pixel. Once this analysis is run for the 10^6 pixels in each stack, we produce proportion maps for the three components ($ACC \cdot H_2O$, ACC, or calcite). Thus for each pixel, the sum of proportions in three proportion maps is always 1. All proportion maps presented here were re-

scaled so the pixels in which the Ca spectra have intensity below a user-specified value (30–45 in the case of Figs. 2 and 3, thus eliminating all pixels from epoxy areas) are removed. The higher-Ca-intensity pixels are retained, and their proportion (between 0 and 1) in each of the three proportion maps is rescaled between 0 and 255. We enhanced the brightness of each pixel, so the brightness is maximum in the dominant channel. Specifically, if a pixel has amounts of red (r), green (g) and blue (b), with r, g, and b varying between 0 and 255 in these 8-bit images, we transformed them from [r g b] to [R G B], where

$$R = 255^{*}r/m \qquad G = 255^{*}g/m \qquad B = 255^{*}b/m,$$

where m is the maximum amount among the r, g, and b values in each pixel.

The resulting RGB map is a brightness-enhanced RGB image. All RGB maps presented here were brightness-enhanced.

The three rescaled, brightness-enhanced proportion maps are then saved as .tif files, and loaded as grayscale into Adobe Photoshop, such that the ACC · H_2O proportion map went into the red channel, the ACC map into the green channel, and the calcite map into the blue channel. We then merged the three RGB channels to obtain an RGB map.

We also did 4-component mapping, including a damage component, as described in Fig. S10 caption. The results of 3-component and 4-component RGB maps were indistinguishable to the naked eye, demonstrating that there is no significant damage to the spicule minerals, and that the results of Figs. 2, 3, and S5 cannot be artifacts of radiation damage (see Fig. S10).

The data presented in Table S2 were calculated from the spicule component analysis maps in Fig. 3. Pixel intensities (0–255) were summed for every pixel in a single color channel (Red, Green, and Blue) for each group of spicules.

1. Radha AV, Forbes TZ, Killian CE, Gilbert PUPA, Navrotsky A (2010) Transformation and crystallization energetics of synthetic and biogenic amorphous calcium carbonate. *Proc Natl Acad Sci USA* 107:16438–16443.
2. Killian CE, et al. (2009) The mechanism of calcite coorientation in the sea urchin tooth. *J Am Chem Soc* 131:18404–18409.
3. Foltz KR, Adams NL, Runft LL (2004) Echinoderm eggs and embryos: Procurement and culture. *Methods Cell Biol* 74:40–71.
4. Sand KK, et al. (2010) Binding of ethanol on calcite: The role of the OH bond and its relevance to biomineralization. *Langmuir* 26:15239–15247.
5. De Stasio G, Frazer BH, Gilbert B, Richter KL, Valley JW (2003) Compensation of charging in X-PEEM: A successful test on mineral inclusions in 4.4 Ga old zircon. *Ultramicroscopy* 98:57–62.
6. Puig O, et al. (2001) The tandem affinity purification (TAP) method: A general procedure of protein complex purification. *Methods* 24:218–229.
7. Mann K, Wilt FH, Poustka A (2010) Proteomic analysis of sea urchin (*Strongylocentrotus purpuratus*) spicule matrix. *Proteome Sci* 8:33.
8. Raz S, Hamilton PC, Wilt FH, Weiner S, Addadi L (2003) The transient phase of amorphous calcium carbonate in sea urchin larval spicules: The involvement of proteins and magnesium ion in its formation and stabilization. *Adv Funct Mater* 13:1–8.
9. Gilbert PUPA, et al. (2008) Gradual ordering in red abalone nacre. *J Am Chem Soc* 130:17519–17527.
10. Frazer BH, Girasole M, Wiese LM, Franz T, De Stasio G (2004) Spectromicroscope for the photoelectron imaging of nanostructures with X-rays (SPHINX): Performance in biology, medicine and geology. *Ultramicroscopy* 99:87–94.
11. GG-Macros (2011) http://home.physics.wisc.edu/gilbert/.

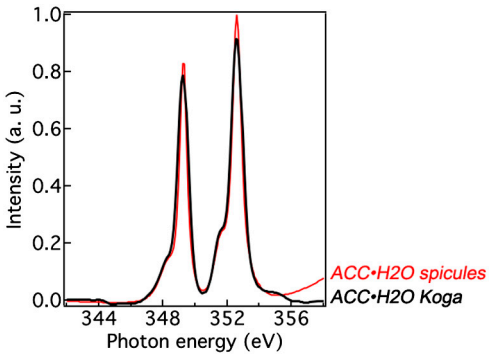

Fig. S1. Comparison of XANES spectra extracted from spicules (red) and from a reference standard compound, ACC · H_2O, prepared with the Koga method (1) (black). The similarity of the two spectra supports our present interpretation, and that of Politi et al. (2) that this amorphous phase in spicules is hydrated ACC. The ACC · H_2O Koga spectrum is from ref. 2, as presented in their figure 1E, top spectrum. The ACC · H_2O spicules spectrum is from this work, and is the result of peak fitting the averaged spectra from six independently acquired 20-nm pixels, as shown in Fig. S2.

1. Koga N, Nakagoe YZ, Tanaka H (1998) Crystallization of amorphous calcium carbonate. *Thermochim Acta* 318:239–244.
2. Politi Y, et al. (2008) Transformation mechanism of amorphous calcium carbonate into calcite in the sea urchin larval spicule. *Proc Natl Acad Sci USA* 105:17362–17366.

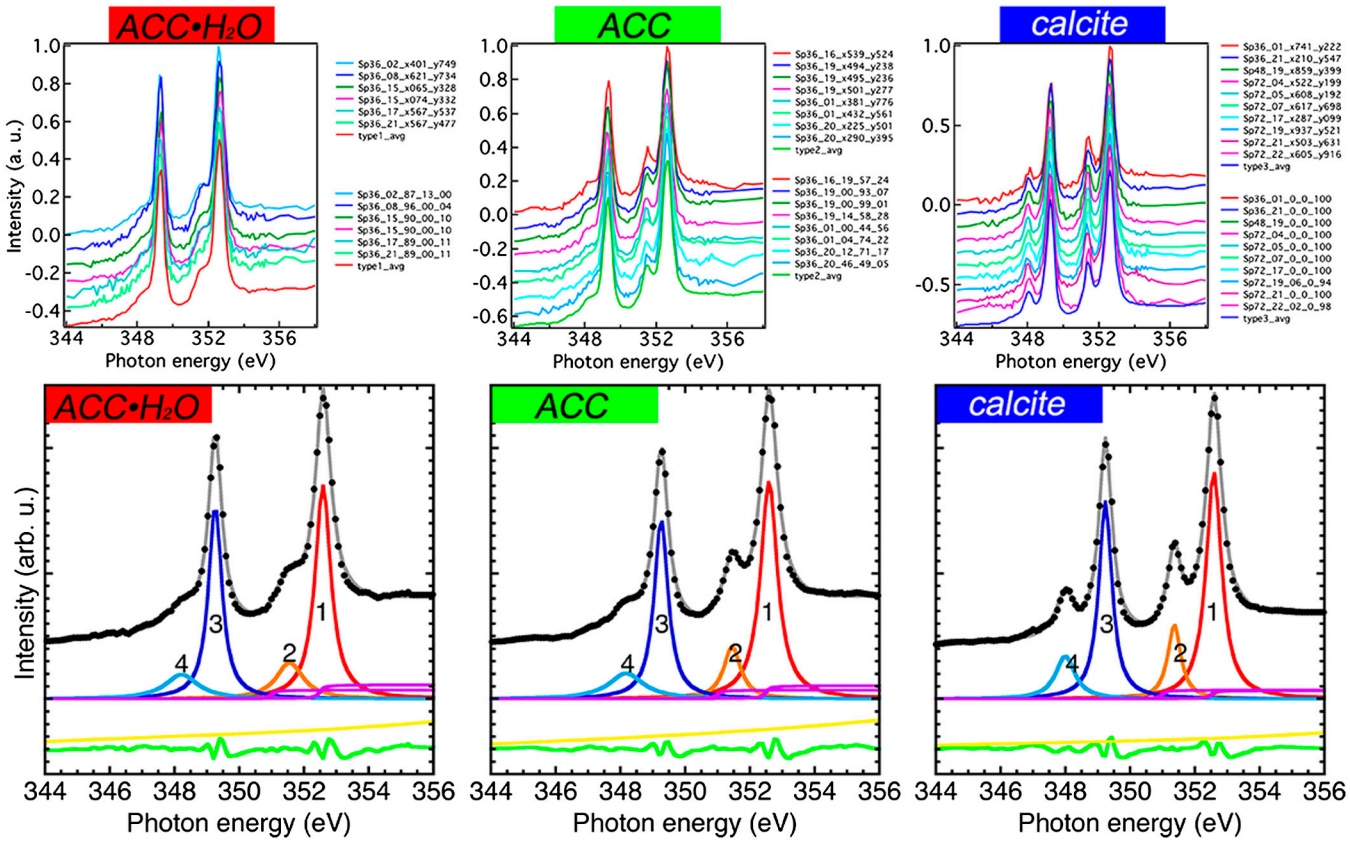

Fig. S2. (*Top*) Averaging and peak fitting of raw spectra to obtain noise-free reference spectra. The top three plots show that for ACC · H_2O, ACC, and calcite we used 6, 8, and 10 raw spectra, respectively, from 20-nm pixels in 36-h, 48-h, or 72-h spicules. Each plot shows two sets of legends corresponding to the same spectra: The top legends show the age of the spicules, the stack number, and the *x* and *y* coordinates of the single pixel from which they were extracted. The bottom set of legends shows spicule age, stack number, and the percentage of ACC · H_2O, ACC, and calcite, respectively, contained in that pixel. For ACC · H_2O and ACC we selected the pixels that gave the greatest ACC · H_2O or ACC percentage, on the order of 90%, in 36-h spicules. For calcite we selected pixels that gave nearly 100% calcite, as most pixels do in 72-h spicules. Each plot shows the average spectrum at the bottom in the red, green, and blue solid lines, respectively. These average spectra were then peak-fitted as shown in the bottom three plots. (*Bottom*) The averaged-spectra data (same as above) are now plotted as black data points, and the fits as solid gray lines. These fits were obtained using four Lorentzian peaks, two arctan, and a third order polynomial. The residues are plotted in green. These are the differences between the experimental data and the results of the peak fitting (black dots and gray lines). The polynomial (yellow) and the residue (green) are displaced down, whereas the data and the fit are displaced up for clarity. All fit components are plotted in different colors. The peak labels 1, 2, 3, 4 are kept at identical positions in all plots to highlight variations in peak intensities and positions. Notice the dramatic increase in the intensity of peak 2 upon dehydration (ACC · H_2O → ACC) and crystallization (ACC → calcite), and of peak 4 upon crystallization (ACC → calcite). There is also a significant shift of peaks 2 and 4 toward lower energies with dehydration and crystallization. See Table S1 for all fit parameters.

Table S1. All fit parameters obtained from the peak-fitting in Figs. 1 and S2

		ACC · H_2O	ACC	Calcite
Background third order polynomial	p0	0.063	0.061	0.033
	p1	0.0057	0.0076	0.0034
	p2	0.00028	0.00028	0.00023
	p3	3.33E-05	1.49E-05	2.73E-05
Lorentzian peak 1	position	352.59	352.59	352.59
	height	0.85	0.87	0.90
	width	0.59	0.64	0.58
Lorentzian peak 2	**position**	**351.56**	**351.45**	**351.37**
	height	**0.14**	**0.21**	**0.30**
	width	1.00	0.63	0.48
Lorentzian peak 3	position	349.26	349.26	349.24
	heigth	0.75	0.71	0.79
	width	0.50	0.52	0.49
Lorentzian peak 4	**position**	**348.22**	**348.18**	**348.00**
	height	**0.10**	**0.11**	**0.17**
	width	1.23	1.30	0.72
Ionization potential arctan 1	position	351	351	351
	height	0.04	0.04	0.04
	width	0.2	0.2	0.2

		ACC · H_2O	ACC	Calcite
Ionization potential arctan 2	position	352.5	352.5	352.5
	height	0.06	0.05	0.03
	width	0.2	0.2	0.2

Notice the most relevant changes highlighted in bold. There is a dramatic increase in the intensity of peak 2 with dehydration and crystallization (from 0.14 to 0.21 to 0.30), and an increase of peak 4 intensity with crystallization (0.11 to 0.17). There is also a significant shift of peaks 2 and 4 toward lower energies with both dehydration and crystallization.

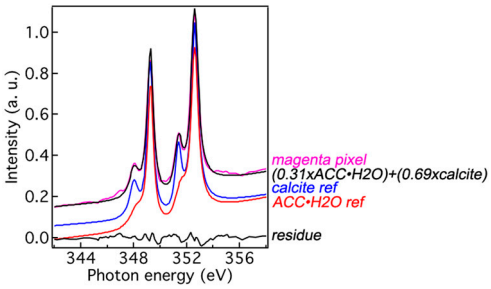

Fig. S3. XANES spectrum (magenta) from one of the magenta 20-nm pixels in Fig. 3. According to the fit results, this portion of the spicule contains 31% ACC · H_2O, no ACC, and 69% calcite. The magenta pixel spectrum is overlapped with a linear-combination-spectrum (black), obtained adding 31% ACC · H_2O spectrum (red) and 69% calcite spectrum (blue). The black and magenta spectra overlap nicely, as demonstrated by the small residue (bottom curve), which is the difference of the two curves, and contains only noise.

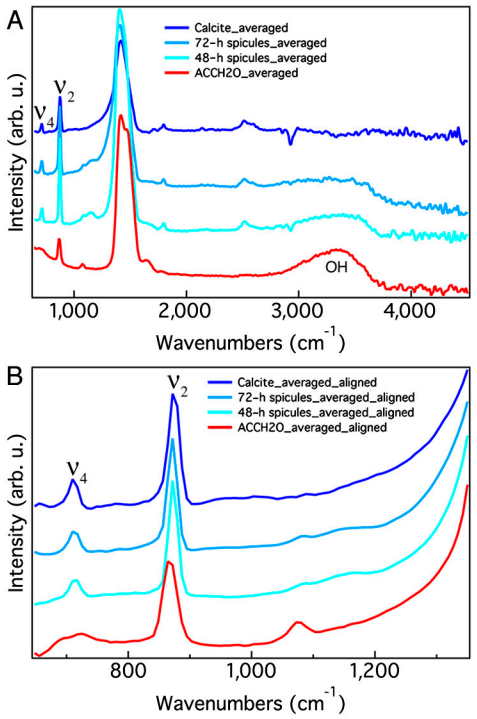

Fig. S4. Attenuated total internal reflection Fourier transform infrared (ATR-FTIR) spectra of 48-h and 72-h fresh spicules, compared to geologic calcite and synthetic ACC · H_2O. (*A*) Full-range ATR-FTIR spectra showing the ν_2 and ν_4 peaks (at 871 cm^{-1} and 711 cm^{-1}, respectively) characteristic of $CaCO_3$, as well as the OH peak characteristic of H_2O. Each spectrum is the average of two or more spectra acquired in different regions of the same sample, and includes many spicules or powder grains. The OH peak shows abundant water in ACC · H_2O (0.017 absorbance units), no water in calcite (0.000), and intermediate water concentrations in 48-h and 72-h spicules (0.009 and 0.008, respectively). (*B*) Same spectra as in *A*, showing only the region of ν_2 and ν_4 peaks. These spectra were aligned in the energy range displayed only, by subtracting the background, that is a third order polynomial fit to each spectrum after masking-off the ν_2 and ν_4 peaks. After this alignment, the intensity ratio of the ν_2 and ν_4 peaks $I(\nu_2)/I(\nu_4)$ is 3.9 for calcite, 5.3 for 72-h spicules, 6.6 for 48-h spicules, and 7.4 for ACC · H_2O. The spectra in both *A* and *B* are displaced vertically for clarity.

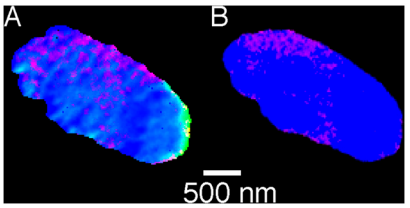

Fig. S5. (*A*) Cross-section of a 48-h (prism stage) sea urchin spicule, imaged and spectroscopically analyzed by XANES-PEEM, 4 d after extraction from the embryo. The pixels are 20 nm. The RGB map is color coded as in Figs. 2 and 3, thus according to additive color mixing (1) red + green = yellow, green + blue = cyan, and red + blue = magenta. Because the red component is present in much lower concentrations, the red level was digitally enhanced, as described in the *SI Methods*, to increase visibility of the magenta nanoparticles. Notice the amorphous phases at the right-hand side edge of the spicule, and the amorphous+crystalline nanoparticles (magenta) inside the spicule cross-section. (*B*) The same spicule in *A*, analyzed again 2 mo later, after storing the sample in a desiccator at room temperature. The ACC at the outer rim had fully crystallized, but magenta nanoparticles persist.

1. Gilbert PUPA, Haeberli W (2011) *Physics in the Arts, Revised Edition*, Complementary Science (Elsevier-Academic, Burlington, MA).

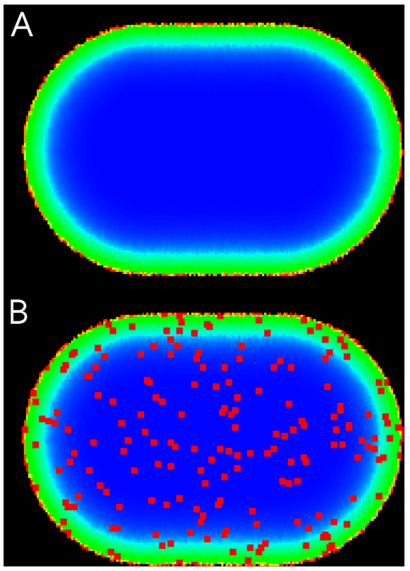

Fig. S6. The RGB maps generated by the model simulation of a forming spicule (*A*) without and (*B*) with an ACC · H_2O → ACC inhibitor. These results correspond to hypotheses 1–8 and 1–9, respectively. In both RGB maps, we note the expected features observed experimentally with XANES-PEEM: red ACC · H_2O exists at the outermost edge of the spicule; immediately inside the outer edge is green ACC; and at the center of the spicule there is mostly calcite. Notice that only the model with inhibitor (*B*) shows ACC · H_2O nanoparticles throughout the model spicule cross-section, as in the experiment of Fig. S5. See animated versions of these model forming spicules in Movies S1 and S2.

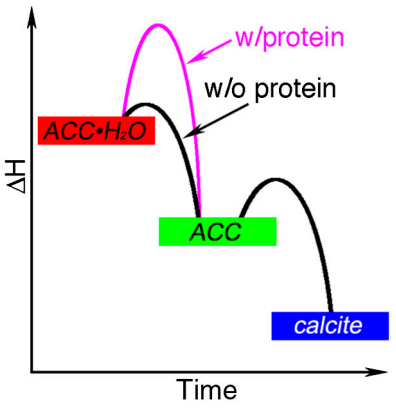

Fig. S7. Proposed energy landscape of the transitions between ACC · H_2O (state at highest, most metastable energy) → ACC → calcite (stable). The relative energy positions are based on the measured values of enthalpy (1). Activation barriers of unknown nature separate the three states. In this schematic representation, the height of each barrier represents a parameter inversely proportional to the transition time. Notice that in the absence of inhibiting protein the activation barrier for ACC · H_2O → ACC is much smaller than for ACC → calcite. In synthetic ACC · H_2O the height of these barriers is reversed (2).

In biogenic ACC, in the presence of inhibiting protein the barrier is much greater (magenta).

1. Radha AV, Forbes TZ, Killian CE, Gilbert PUPA, Navrotsky A (2010) Transformation and crystallization energetics of synthetic and biogenic amorphous calcium carbonate. *Proc Natl Acad Sci USA* 107:16438–16443.
2. Raiteri P, Gale JD (2010) Water is the key to nonclassical nucleation of amorphous calcium carbonate. *J Am Chem Soc* 132:17623–17634.

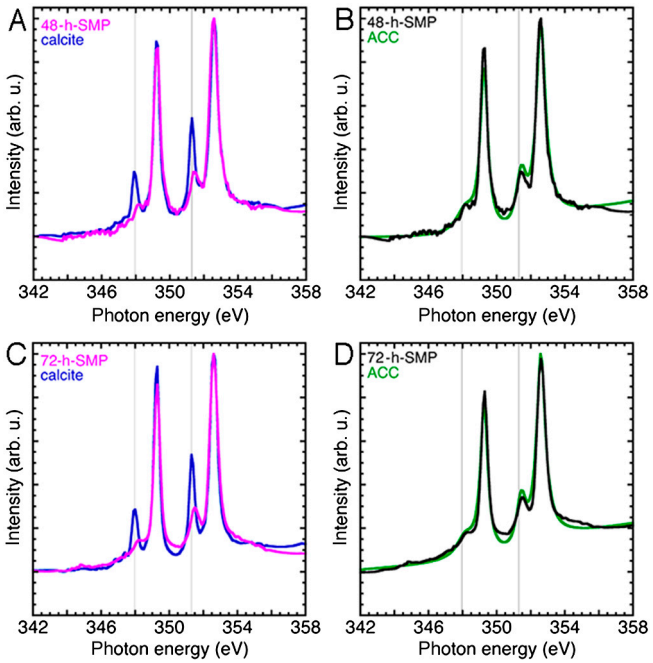

Fig. S8. Additional spectra obtained from the in vitro assay of protein functions described in the text. (*A* and *C*) Integral SMP extracted from 48-h (prism stage) and 72-h (pluteus stage) embryos of *S. purpuratus*. The spectra acquired from 48-h SMP or 72-h SMP dried-droplets on calcite are shown in magenta and compared with calcite (blue). The reprecipitate in the presence of all proteins in the spicule, whether 48 h or 72 h, is clearly not calcite but dehydrated ACC. (*B* and *D*) Comparison of the spectra in *A* and *C* with the reference dehydrated ACC (green).

The spectra are very similar, demonstrating that one or more spicule matrix proteins stabilize anhydrous ACC, even in direct contact with a crystalline calcite wafer. This observation is in agreement with previous experiments by the Addadi–Weiner group (4). ACC stabilization by spicule matrix proteins explains the long-lived ACC phase observed in Fig. S5*A*, although we do not know at present which ones, among the 218 spicule matrix proteins identified by Mann et al. (7) stabilize dehydrated ACC.

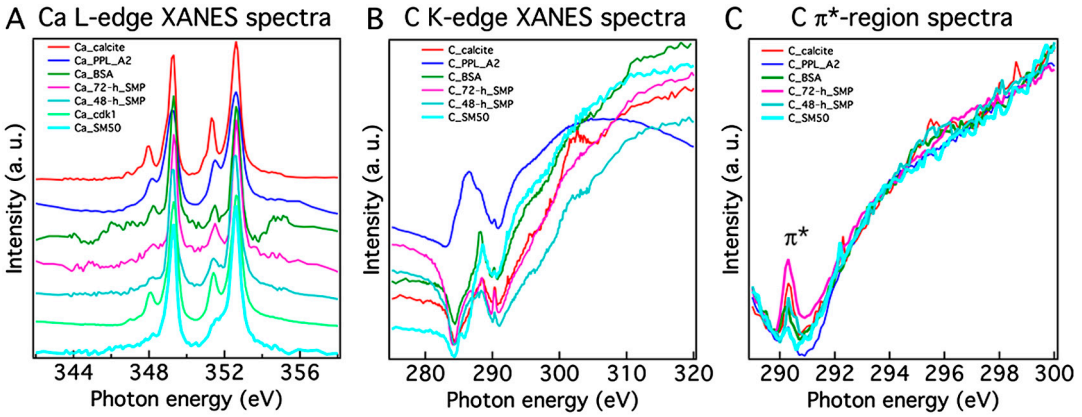

Fig. S9. XANES spectra for all proteins in Figs. 4 and S8, and the calcium L-edge (*A*) and carbon K-edge (*B*, *C*) edges, acquired from the exact same region in each sample. In all cases a region of dried protein droplet on calcite was analyzed. All $CaCO_3$ species, whether amorphous or crystalline, exhibit the carbonate π^* peak in the unnormalized carbon spectra in *B*. The π^* peak at 290.3 eV is magnified in *C*, where the spectral backgrounds were aligned to overlap as much as possible. The C spectrum for cdk1 was not acquired, because the Ca spectrum shows that the reprecipitate is clearly calcite. A technical comment for the spectromicroscopist: The presence of the π^* peak was deemed sufficient to identify the existence of a carbonate cluster. Notice that in the amorphous species (SM50, 48-h SMP, 72-h SMP) the carbonate π^* peak cannot originate from the calcite substrate. If photoelectrons at the carbon π^* originated from the underlying calcite crystal, then in the same exact regions photoelectron at the calcium L-edge would come from even deeper into the crystal because their initial kinetic energy is greater (1). In this case they should show the characteristic calcite crystal field peaks in the Ca spectra, and they clearly do not. Therefore, in both Ca and C spectra the signal originates from reprecipitated carbonates at the surface of the dried protein droplets.

1. Frazer BH, Gilbert B, Sonderegger BR, De Stasio G (2003) The probing depth of total electron yield in the sub keV range: TEY-XAS and X-PEEM. *Surf Sci* 537:161–167.

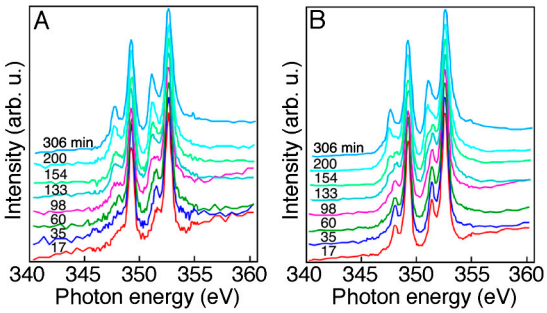

Fig. S10. The effect of radiation damage on Ca spectra from 48-h (prism stage) spicules. (*A*) Single-pixel XANES spectrum from a 20-nm pixel originally containing mostly amorphous phases (53% ACC · H_2O, 35% ACC, and only 7% calcite). The first spectrum at the bottom was acquired with a total exposure time of 17 min. The others were acquired after exposing for the indicated lengths of time, in minutes. (*B*) XANES spectra from a 20-nm pixel originally containing 100% calcite in the 17-min spectrum. Both pixels in *A* and *B*, after long exposure times, show CaO spectra. At shorter exposure times, e.g., 60 min (dark green spectrum in *A*), ACC has effectively transformed into calcite. With increasing time of X-ray beam exposure, ACC · H_2O transforms into ACC, which subsequently transforms into calcite. Calcite then transforms into CaO and CO_2. The effect of radiation damage starts to appear spectroscopically after 35 and 98 min of exposure, respectively, for ACC and calcite pixels. The 306-min spectra in both plots are pure CaO, with no residual calcite. The data of Figs. 2 and 3 were acquired with exposure time of 20 min or less, hence their spectroscopic results should not be affected by radiation damage to carbonates. In addition, we repeated the component mapping in Figs. 2 and 3–48 h using four components. The fourth component is the pure CaO spectrum of the most damaged 306-min spectrum shown here. Only a small percentage of each pixel spectrum contained any CaO, and CaO pixels were usually colocalized with the amorphous phases, indicating their greater sensitivity to damage. ACC · H_2O-rich and ACC-rich pixels always contained <20% CaO, whereas calcite-rich pixels had <1% CaO. A comparison between 3- and 4-component mapping of the spicules in Figs. 2 and 3 did not show qualitative differences. Spectroscopic differences observed here are not due to crystal orientation and linear dichroism effects because we used circularly polarized light to correct for that possibility.

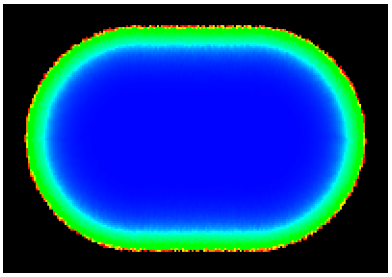

Movie S1. Cross-section of a forming spicule, simulated without any ACC · H_2O → ACC inhibitor. As the spicule grows, more red ACC · H_2O is deposited at the outer rim, and they gradually transforms into green ACC and then into blue calcite. This simulation follows hypotheses 1–8.

Movie S1 (MOV)

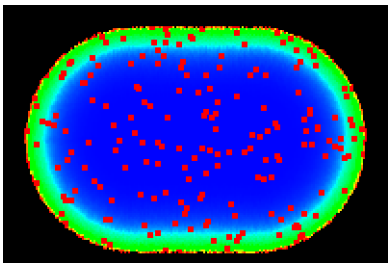

Movie S2. Simulated RGB map of a forming spicule with ACC · H_2O → ACC inhibitor, thus including hypothesis 9: In the presence of inhibitor, ACC · H_2O will not transform into ACC. The randomly distributed inhibitors are present in 1% of the pixels, and each inhibitor affects a 3×3 pixel region. Notice that this simulation shows long-lived ACC · H_2O nanoparticles throughout the model spicule cross-section, as found in the experiment of Fig. S5.

Movie S2 (MOV)

Table S2. Quantitative analysis of ACC · H_2O (red), ACC (green), and calcite (blue) as identified from the Ca spectroscopy and component mapping in all the spicules of Fig. 3

Spicule age (h)	Color channel	Total no. of pixels	Total (%)
36	red	17788188	40
36	green	8538670	20
36	blue	17399907	40
48	red	3967073	9
48	green	15111247	32
48	blue	27237947	59
72	red	427200	1
72	green	20735	0
72	blue	58518089	99

Notice that in 36-h, 48-h, and 72-h spicules the $CaCO_3$ present is 60, 41, and 1% amorphous, whereas 40, 9, and 1% is ACC · H_2O. Regarding water, we stress that the latter results only apparently indicate less water than expected, based on previous analysis (1, 8). Water not in the immediate vicinity of Ca atoms would go undetected in XANES spectra at the Ca edge. Hence these results should be interpreted not as water-content analysis, but as calcium-nearest-neighbor-water analysis. The FTIR data of Fig. S4 yield bulk-water analysis, whether this water is near or far from Ca atoms.